

# CrystalFormer-RL: Reinforcement Fine-Tuning for Materials Design

Zhendong Cao<sup>1,2</sup> and Lei Wang<sup>1,3,\*</sup>

<sup>1</sup>Beijing National Laboratory for Condensed Matter Physics and Institute of Physics,  
Chinese Academy of Sciences, Beijing 100190, China

<sup>2</sup>School of Physical Sciences, University of Chinese Academy of Sciences, Beijing 100190, China

<sup>3</sup>Songshan Lake Materials Laboratory, Dongguan, Guangdong 523808, China

(Dated: April 4, 2025)

Reinforcement fine-tuning has instrumentally enhanced the instruction-following and reasoning abilities of large language models. In this work, we explore the applications of reinforcement fine-tuning to the autoregressive transformer-based materials generative model CrystalFormer (arXiv:2403.15734) using discriminative machine learning models such as interatomic potentials and property prediction models. By optimizing reward signals—such as energy above the convex hull and material property figures of merit—reinforcement fine-tuning infuses knowledge from discriminative models into generative models. The resulting model, CrystalFormer-RL, shows enhanced stability in generated crystals and successfully discovers crystals with desirable yet conflicting material properties, such as substantial dielectric constant and band gap simultaneously. Notably, we observe that reinforcement fine-tuning enables not only the property-guided novel material design ability of generative pre-trained model but also unlocks property-driven material retrieval from the unsupervised pre-training dataset. Leveraging rewards from discriminative models to fine-tune materials generative models opens an exciting gateway to the synergies of the machine learning ecosystem for materials.

## I. INTRODUCTION

In materials science, machine learning (ML) techniques are revolutionizing research to enable rapid design and discovery of materials with desired properties. Machine learning models can be broadly categorized into generative and discriminative approaches. Crystal generative models, aim to capture the prior probability distribution  $p(x)$  of stable crystal structures in the chemical space, learning the underlying patterns and correlations in crystal data to generate novel structures. These generative models [1–6] capture the underlying distribution of stable materials in the chemical space and enable the direct generation of novel materials. On the other hand, discriminative models, including machine learning interatomic potentials (MLIP) [7–13] and property prediction models [14, 15], focus on modeling the conditional probability  $p(y|x)$ , where  $y$  represents material properties given a crystal structure  $x$ . These models excel at predicting specific properties or behaviors of materials and enable accelerated simulations and property predictions. The integration of these complementary approaches—combining the generative capability of models that capture  $p(x)$  with the predictive power of discriminative models that capture  $p(y|x)$ —presents a powerful framework for materials discovery. Further achievements hinge on the flexible combination of discriminative and generative models, enhancing their performance and adapting them to specific application domains. Reinforcement learning (RL) provides a principled way to achieve this synergy, allowing the generative model to be improved and guided by the knowledge embedded in discriminative models.

The synergy of discriminative and generative machine learning models has already shown great success in real-world applications in the past few years. A notable example is classifier-guided generation [16, 17], where supervised

trained discriminative models are leveraged to guide sampling of generative models, eliminating the need for iterative retraining of the generative model. Moreover, in the post-training phase of large language models (LLM), reinforcement learning from human feedback (RLHF) [18, 19] is employed to extract signals from supervised trained reward models to instruct generative models. In this context, RL [20] serves as a powerful mechanism to integrate unsupervised and supervised learned models. For example, LLM trained via RL have demonstrated improved instruction following [18] and reasoning capabilities [21], which shows it is an effective way to enhance the performance of generative models.

Inspired by RLHF, we devise an RL approach to finetune the crystal generative model CrystalFormer using discriminative models such as MLIP and property prediction models, see Fig. 1(a). We demonstrate that the approach effectively enhances the stability and desired figures of merit of generated materials. We have released the codes and trained models at [22]. Moreover, we provide instructions on fine-tuning CrystalFormer with customized MLIP or property prediction models other than the ones used in this work.

The organization of the paper is as follows: Section II describes the RL algorithm for fine-tuning CrystalFormer. Section III presents the results on improving the stability of generated materials and examples of property-controlled material generation. Section IV discusses the prospects of this work in a broader context.

## II. METHOD

In the spirit of RLHF [18, 19], we fine tune pre-trained crystal generative model using reward signal from MLIP or a material property prediction model. The objective function to be maximized reads [23],

$$\mathcal{L} = \mathbb{E}_{x \sim p_{\theta}(x)} \left[ r(x) - \tau \ln \frac{p_{\theta}(x)}{p_{\text{base}}(x)} \right], \quad (1)$$

\* wanglei@iphy.ac.cn

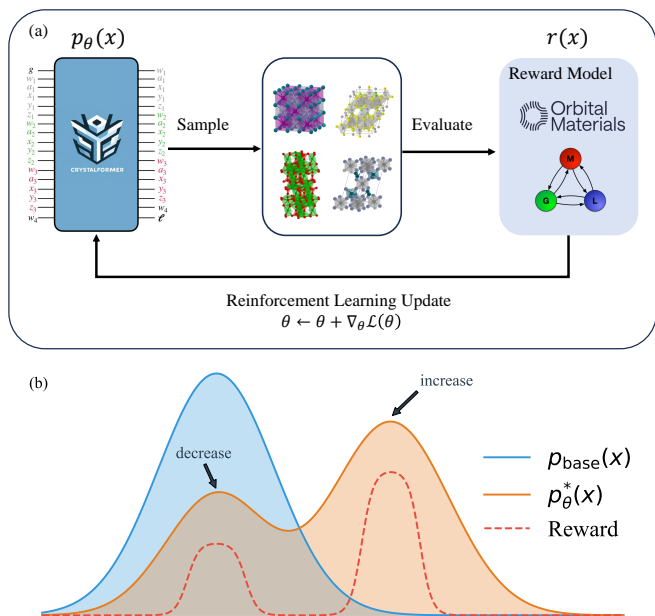


Figure 1. (a) The reinforcement fine-tuning workflow. Machine learning interatomic potential or property prediction models provide rewards to the material generated by CrystalFormer. The RL training loop updates the parameters of a pre-trained CrystalFormer to maximize the objective function in Eq. (1). (b) The reinforcement fine-tuned model deviates from the base model to maximize the expected reward with entropy regularization.

where  $x$  represents crystalline materials sampled from a policy network  $p_\theta(x)$ ,  $r(x)$  is the reward function which awards preferred materials with high returns,  $\tau$  is the regularization coefficient controls proximity to the base model  $p_{\text{base}}(x)$ . The second term of Eq. (1) is the Kullback-Leibler (KL) divergence between the policy distribution and the base model [24]. Overall, the objective function aims to maximize the expected reward of samples while ensuring that the policy also aligns with the base model.

The combination of both terms in Eq. (1) can also be regarded as a KL divergence between the policy network  $p_\theta(x)$  under fine-tuning and an optimal policy [23, 25]

$$p_\theta^*(x) = \frac{p_{\text{base}}(x)}{Z} \exp\left(\frac{r(x)}{\tau}\right), \quad (2)$$

where  $Z$  is the normalization factor. The corresponding optimal value of the objective function Eq. (1) will be  $\tau \ln Z$ . Setting the reward to be proportional to the log-likelihood of certain desired property  $r(x) \propto \tau \ln p(y|x)$ , one sees that  $p_\theta^*(x) \propto p_{\text{base}}(x)p(y|x)$ . Therefore, Eq. (2) can be viewed as Bayesian inference with a prior distribution  $p_{\text{base}}(x)$  and the likelihood  $\exp(r(x)/\tau)$  [25, 26]. The pre-trained model not only provides the prior distribution  $p_{\text{base}}(x)$  but also provides parameter initialization for the policy network. Figure 1(b) illustrates the RL fine-tuning process. The variational inference provides an alternative to the Markov chain Monte Carlo (MCMC) sampling carried out in Ref. [5]. Here, larger  $\tau$  corresponds to higher temperature and hence stronger entropy

regularization. Such optimization is also equivalent to the variational free energy calculations carried out for statistical mechanics problems [27, 28], where the two terms in the objective function Eq. (1) correspond to expected energy and entropy, respectively. We employ the proximal policy optimization (PPO) [29] algorithm to maximize the expected reward. The implementation details are provided in Appendix C.

In the RLHF paradigm for LLM, a reward model that represents human preferences is used to evaluate the quality of generated samples. Analogously, in computational material science, density functional theory (DFT) is frequently employed to assess the quality of crystalline materials. However, the computational expense associated with DFT renders its direct application as a reward model within the RLHF framework infeasible. To circumvent this limitation, we propose the utilization of an MLIP as a surrogate reward model. Recent advancements in MLIP have yielded models capable of simulating atomic systems with both high accuracy and reduced computational cost, thus providing a viable proxy for DFT calculations [7]. Moreover, universal MLIP [11–13, 30–32], encompassing the entire periodic table of chemical elements, offering the capacity to evaluate a diverse range of materials, making them particularly well-suited for our RL fine-tuning.

RLHF can also be effectively employed for property-guided material generation, wherein the reward model is one or a combination of several property prediction models [33–36]. The fine-tuned generative model is capable of generating materials with desired properties, such as band gap, formation energy, and so on. We choose to carry out RL fine-tuning for the crystal generative model CrystalFormer [5] due to its simplicity, generality, and flexibility.

The CrystalFormer is an autoregressive transformer which models the tokenized representation of crystal structures with explicit knowledge of space group symmetries. The representation includes the space group number, Wyckoff letter, chemical element, and fractional coordinates of each symmetry inequivalent atom, and finally, the lattice parameters of the unit cell [5]. For example, the crystal LaH<sub>10</sub> in the  $Fm\bar{3}m$  (No. 225) space group with the cubic conventional unit cell of the length 5.1Å is represented as the sequence "225-a-La-0-0-0-c-H-1/4-1/4-1/4-f-H-0.375-0.375-0.375-X-5.1-5.1-5.1-90-90-90", which contains all the necessary information of the crystal. Key to the design of CrystalFormer is the sequential nature of Wyckoff letters which decrease in site symmetry in an alphabet order. In this regard, the CrystalFormer leverages Nature’s codebook—the Wyckoff position table—for a multimodal probabilistic modeling. Although the representation appears to lack a sense of spatial geometry, unsupervised pre-training allows the model to ingest solid-state chemistry knowledge by compressing the crystalline material database into the model parameters. Furthermore, the RL phase may allow it to extract the geometry and physics from MLIP and property prediction models trained with supervised approaches.

In the present work, we first train the CrystalFormer on the Alex-20 dataset, which is curated from the Alexandria dataset [37]. More details of the dataset can be found in the Appendix B. The resulting pre-trained model then serves as

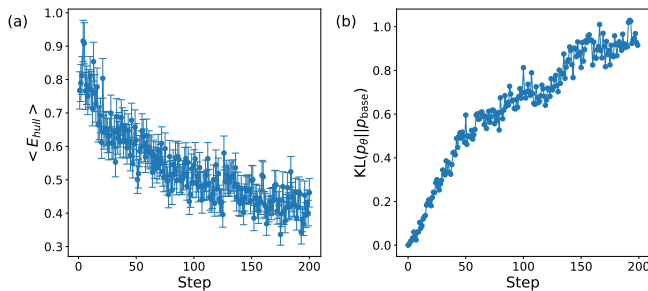


Figure 2. (a) The average energy above the convex hull of generated materials and (b) the KL divergence between the policy and the base model versus training steps. We set the regularization coefficient  $\tau = 0.1$ .

the base model for the RL procedure, where we fine-tune the model using the RL method using the MLIP or crystal property prediction models as the reward model. In the RL stage, the model learns from the reward model on its own samples. We sample crystal structures from CrystalFormer’s policy,  $p_{\theta}(x)$ , with the space groups distributed according to the Alex-20 dataset. The samples are then evaluated by the reward model  $r(x)$ , which assigns a reward based on stability or properties. These reward signals provide feedback for updating the CrystalFormer’s policy to maximize the objective function in Eq. (1), iteratively improving the CrystalFormer’s capacity to generate target crystal structures. We stop the fine-tuning process when the loss function converges.

### III. APPLICATIONS

#### A. Reinforcement learning from MLIP for improved stability of generated materials

As the first application of the reinforcement fine-tuning of CrystalFormer, we choose the energy above the convex hull as the reward signal, i.e.,  $r(x) = -E_{\text{hull}}(x)$ . The energy above the convex hull is the key metric for assessing the stability of a material, with lower values indicating greater stability. To predict the energy and calculate the energy above the convex hull based on the Alexandria convex hull [37], we utilize the Orb model [13]. This choice allows us to obtain accurate energy predictions and assess the stability of materials relative to the convex hull fast. It is important to emphasize that our approach is not limited to the Orb model; any universal MLIP can serve as the reward model. More accurate MLIP yields better reward signals, enhancing alignment with DFT calculations. Benchmarks on universal MLIP such as [38] provide an interactive leaderboard to select the favorable one for the fine-tuning purpose. We evaluate the performance by measuring the fraction of structures that are stable, unique, and novel (S.U.N.) [3]. The stability is defined as the energy above the convex hull being less than 0.1 eV/atom, uniqueness is defined as the generated structure not being identical to any other generated structures, and novelty is defined as the generated

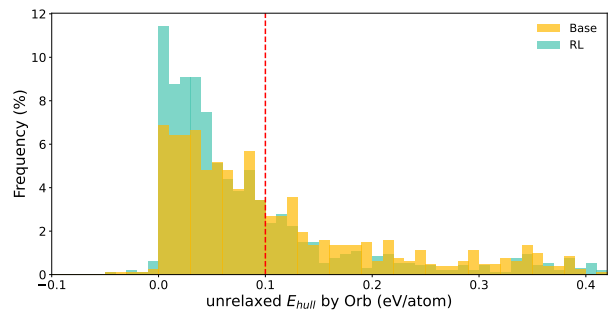


Figure 3. The histogram of energy above convex hull predicted by the Orb model [13] for the crystal samples from the pre-trained and the RL fine-tuned model respectively. The red dashed line indicates the threshold of 0.1 eV/atom. RL finetune improves the ratio of stable materials from 44.7% in the base model to 73.4%.

structure not being present in the training dataset.

Figure 2(a) shows the expected energy above the convex hull of generated samples, which shows steady improvement during the training process. Figure 2(b) shows the KL divergence between the policy and the pre-trained base model  $\text{KL}(p_{\theta} \| p_{\text{base}}) = \mathbb{E}_{x \sim p_{\theta}(x)} \left[ \ln \frac{p_{\theta}(x)}{p_{\text{base}}(x)} \right]$ , which slightly increases during the fine-tuning process.

Figure 3 shows the histogram of the energy above the convex hull for the pre-trained model and the reinforcement fine-tuned model. For each model, 1000 structures were sampled, with their space groups drawn from the training data distribution. We note that we do not relax the generated structures, as the focus of the fine-tuning is to enhance the stability of generated materials. For the pre-trained model, 44.7% of the generated structures are stable, whereas RL improves this ratio to 73.4%, representing a substantial improvement. Simultaneously, the space group symmetry controlled [39] S.U.N. ratio across all generated structures increased from 15.3% for the pre-trained model to 21.6% for the RL fine-tuned model. The results indicate that the RL fine-tuned model generates structures with lower energy above the convex hull compared to the pre-trained base model, suggesting that the RL method effectively optimizes the model to generate more stable structures. Besides reducing the energy above the convex hull, the reinforcement fine-tuning also improves the structure validity metrics compared to the base model [1], see Appendix B.

Figure 4 shows the fraction of generated structures that are stable and are also S.U.N. for 14 space groups spanning the seven crystal systems. We choose to investigate the performance of the model on the same 14 space groups as Ref. [3]. For each space group, we generate 1000 structures and evaluate the quality of samples using the Orb model [13]. The results demonstrate that the reinforcement fine-tuned model generates a higher fraction of stable and S.U.N. structures in most cases, indicating that the RL method can enhance the model’s ability to generate S.U.N. structures even though we only award for the stability function. For space groups with high symmetries (e.g.  $F\bar{4}3m$ ), even though the fraction of stable materials increases, the S.U.N. ratio does not increase possibly due to the restricted degrees of freedom limiting the

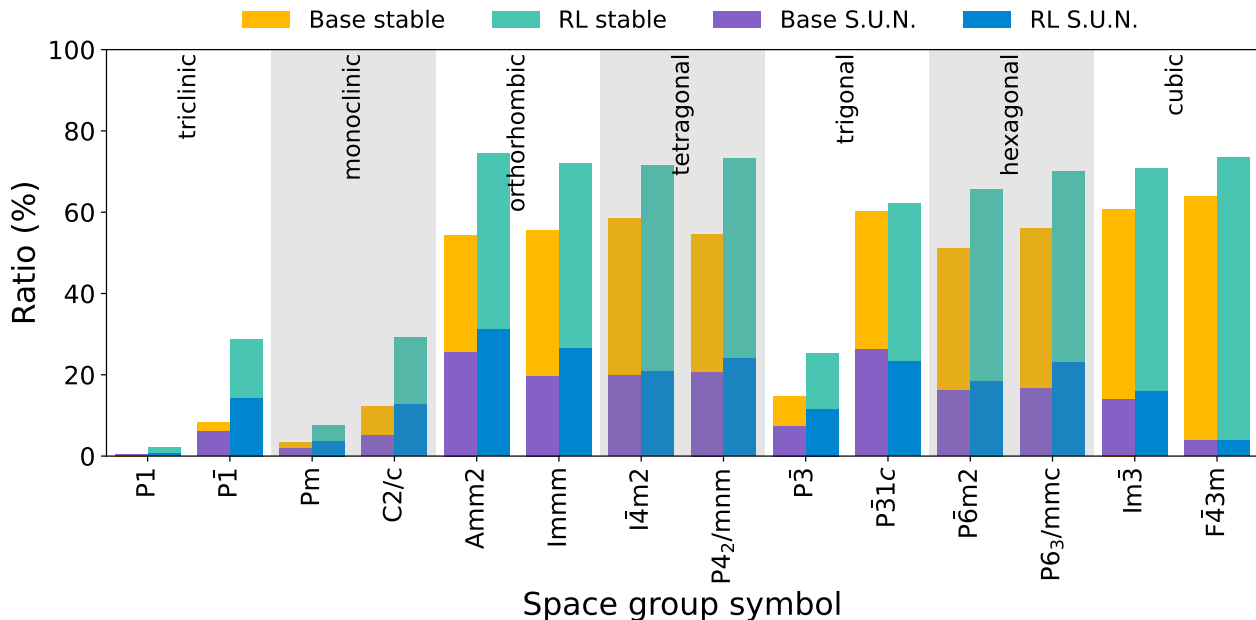


Figure 4. Fraction of generated structures that are stable, and are also S.U.N. for 14 space groups spanning the seven crystal systems.

structural motifs. From the figure one also observes that the performance of `CrystalFormer` is worst for the  $P1$  space group where there is minimal symmetry-related inductive bias to be explored. This is in sharp contrast to Ref. [3] which shows the best S.U.N. in the  $P1$  space group. In fact, for space group with higher symmetry which are more relevant to the natural distribution of inorganic materials [40], we observed that the performance of `CrystalFormer` is on par or even better than the ones shown in Fig. D8 of Ref. [3]. Lastly, while reinforcement fine-tuning does not affect the generation speed of the model, it increases the rate of generating S.U.N. samples from 3.46 to 4.89 per second.

Figure 5 breaks down the performance enhancement in terms of the S.U.N. ratio coming from enlarging the pre-training dataset and different ways of fine-tuning. First of all, enlarging the pre-training dataset from MP-20 to Alex-20 yields a significant improvement in the S.U.N. ratio, rising from 2.6% to 15.3%. Next, we also tested the improvement brought by supervised fine-tuning (SFT) on the pre-trained model. For SFT, we generate 10,000 crystal samples and relax them using the Orb models. Only those stable samples with  $E_{\text{hull}} < 0.1$  eV/atom were used to finetune the pre-trained model. Figure 5 shows that SFT yields some improvement over the pre-trained model, further increasing the S.U.N. ratio from 15.3% to 18.3%. However, it is the reinforcement fine-tuned model that delivers the most significant increase in the S.U.N. ratio, leading to a final S.U.N. ratio of 21.6%.

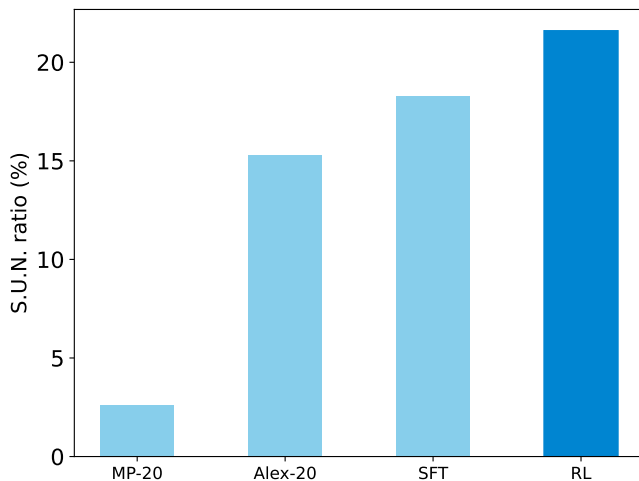


Figure 5. The weighted S.U.N. ratio averaged over all space groups of the `CrystalFormer` trained on the MP-20 dataset and the Alex-20 dataset compared with the fine-tuned model with SFT and RL approaches. The energy above the convex hull is calculated based on the Alexandria convex hull and the novelty is calculated based on the Alex-20 dataset.

## B. Reinforcement learning from the figure of merits for property-guided material generation

Next, we apply the RL method for dielectric material discovery. Dielectric materials are essential components in a wide range of contemporary electronic devices, including flash storage, central processing units, and random access



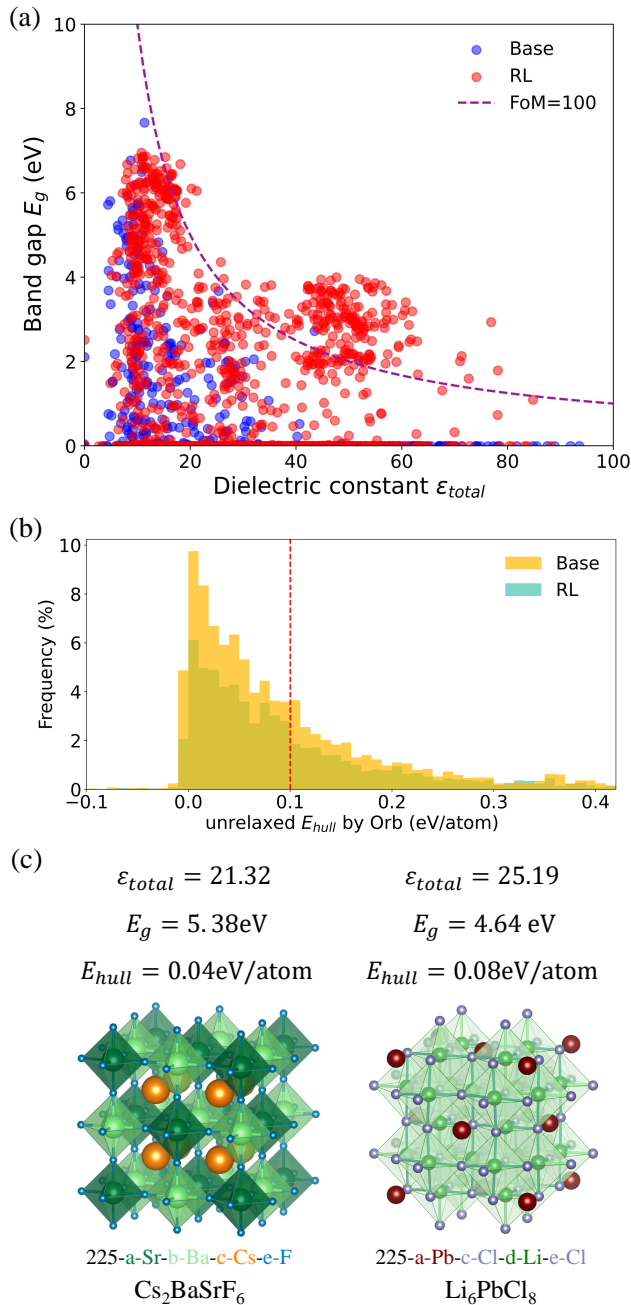


Figure 6. (a) ML-predicted band gap  $E_g$  versus total dielectric constant  $\epsilon_{total}$  for generated samples in the  $Fm\bar{3}m$  space group (No.225). The dashed line indicates a constant figure of merit at values  $\epsilon_{total} \cdot E_g = 100\text{eV}$ . Note that we subsample 1000 data points from the generated samples for better visualization. (b) The histogram of energy above the convex hull predicted by the Orb model [13] for the crystal samples from the pre-trained and the RL fine-tuned model in  $Fm\bar{3}m$  space group (No.225), respectively. The red dashed line indicates the threshold of 0.1 eV/atom. RL improves the FoM of the generated samples towards high FoM dielectric materials at the cost of only slightly affecting the stability. (c) Two examples of discovered high FoM materials along with their properties and tokenized representation (fractional coordinate and lattice parameters omitted).

memory [41, 42]. The functional utility of these materials is fundamentally governed by the precise interplay between the dielectric constant and band gap—two inherently anti-correlated properties that seldom achieve optimality concurrently in a single material. Consequently, delineating a Pareto front becomes essential for navigating the trade-offs between these competing parameters. We utilize the pre-trained MEG-Net [15, 43] model to predict the band gap  $E_g$  for generated samples. The total dielectric constant is a dimensionless number, which is the ratio of the permittivity of a substance to the permittivity of vacuum. To predict the total dielectric constant  $\epsilon_{total}$  which includes the ionic and electronic contributions [44], we train a separate M3GNet [30] model on the dataset of density functional perturbation theory (DFPT) calculations in the Materials Projects [45, 46], more details of training and evaluation can be found in Appendix D. The reward function is defined as the figure of merit (FoM),  $r(x) = \epsilon_{total} \cdot E_g$ , which favors materials with both sizeable band gap and permittivity.

Figure 6(a) shows the ML predicted band gap  $E_g$  versus total dielectric constant  $\epsilon_{total}$  for generated samples in the  $Fm\bar{3}m$  space group (No.225) using the base and fine-tuned model respectively. The reinforcement fine-tuning significantly improves the FoM, with the majority of generated samples exhibiting higher FoM values compared to the pre-trained base model. We observe that the RL method primarily enhances the FoM by increasing the band gap, rather than the dielectric constant. This outcome may be attributed to the limited and relatively low dielectric constant data used to train the dielectric model, potentially causing the model to predict lower dielectric constants. To address this issue, a more robust dielectric prediction model that captures a wider range of dielectric constants could be employed [47]. In contrast, the band gap prediction model demonstrates greater accuracy, resulting in the RL method favoring an increase in the band gap to optimize the FoM.

We generated 5000 samples (which takes 276 seconds with single A100 GPU) and list those with  $E_{hull} < 0.1$  eV/atom and FoM  $> 100\text{eV}$  in Table S2 in Appendix D. We observed that many of these samples are fluoride, probably due to fluorine’s strong electronegativity increases the ionic character of bonds, so that to ensure a sizeable band gap. Moreover, many of these high FoM samples are composed of Cs elements, which may be due to the relatively large ionic radius of Cesium, leading to higher polarizability and thus an increased total dielectric constant of the material. Figure 6(b) shows the energy above the convex hull for the materials sampled from the base and fine-tuned model respectively, which suggests that the reinforcement fine-tuning does not significantly affect the stability of generated materials. Two examples of high FoM materials discovered by CrystalFormer-RL,  $\text{Cs}_2\text{BaSrF}_6$  and  $\text{Li}_6\text{PbCl}_8$ , are shown in Fig 6(c).  $\text{Cs}_2\text{BaSrF}_6$  belongs to the double perovskite [48] structure prototype. We note that although it is flagged as novel in Table S2, it is related to partial substitution [49] of the Ba element in  $\text{CsBaF}_3$  which is in the Alex-20 dataset. Therefore, the synthesis and identification of  $\text{Cs}_2\text{BaSrF}_6$  as a novel compound may subject to caveats pointed out in Ref. [50] such as compositional disor-

der.  $\text{Li}_6\text{PbCl}_8$  is derived from  $\text{Li}_6\text{VCl}_8$  [51] by substituting V with Pb and belongs to the Suzuki structure prototype [52].

Many of the generated samples are present in the Alex-20 dataset which is in line with the S.U.N ratio 5.1% of the base model on space group No.225. This nevertheless demonstrates that the reinforcement fine-tuning procedure can guide the generative process toward discovering candidates within the pretrained dataset with no property label. Notably, 11 materials in Table S2 are *absent* from the Alex-20 dataset, highlighting the ability of RL to guide the generative process toward novel samples beyond the pretrained dataset. We compare the prediction results of the generated samples with that of corresponding equilibrium structures from the Alex-20 dataset in Table S3. We observe that the generated materials are close to the equilibrium structure in the Alex-20 dataset, with similar predicted FoM values.

The CrystalFormer’s ability to aid property-guided exploration of crystalline materials has been demonstrated in previous work [5] using the MCMC sampling method from the posterior distribution according to the Bayes rule. Both the MCMC and reinforcement fine-tuning approach work with any machine learning interatomic potential or property prediction models trained separately of the CrystalFormer. The RL approach addresses the long-mixing time or even the ergodicity issue of the MCMC sampling of the posterior distribution with the additional effort of fine-tuning and a variationally approximated posterior.

#### IV. DISCUSSIONS

Reinforcement fine-tuning of materials generative model is useful for an even broader class of materials properties such as the thermoelectric figure of merit, thermal conductivity, and superconducting critical temperature. In addition to a foundational generative model such as the CrystalFormer for the materials prior  $p(x)$ , the framework requires a reliable ML prediction model for the likelihood  $p(y|x)$ , which is a research topic with rapid progress both on generalizability and accuracy, see, e.g. [53–55].

It is often easier to discriminate the utility of a given material than to generate a material with the desired utility. Reinforcement fine-tuning of a materials generative model using discriminative feedback offers a way to bridge such discrimination-generation gap. RL on the autoregressive transformer such as CrystalFormer [5] is particularly suitable given a variety of post-training techniques available for LLM. Although the RL technique is readily applicable to materials language models [4, 56, 57], we believe finetuned CrystalFormer is more advantageous because it cherishes the fundamental inductive bias of crystalline materials such as space group symmetry and periodicity. Furthermore, many of these RL methods can be extended to the material generative models based on diffusion. The diffusion model is typically fine-tuned through the incorporation of auxiliary networks to condition generation on external inputs [58], while RL eliminates the necessity for these additional network components. For example, Refs. [59, 60] employ the RL algorithm to fine-

tune the pre-trained text-to-image model, leading to improved sample quality and diversity. Nevertheless, applying RL with KL regularization to the diffusion model is challenging due to the need for precise log-likelihood calculations [61].

It is also interesting to compare active learning and RL in the context of generative materials discovery. Active learning [62, 63] selects crystal samples back to the generative training dataset, which is similar to the SFT approach discussed in Sec. III A. The active learning procedure optimizes the same forward KL divergence between the empirical distribution of the training dataset and the generative model. In contrast, RL minimizes the reverse KL divergence [25] between the generative model and the target distribution Eq. (2). There are evidences that the RL approach delivers better performance compared to the active learning approach in the contexts of LLM fine-tuning [64]. Consequently, the primary advantage of RL over active learning is its ability to directly incorporate task-specific reward signals, enabling the model to generate outputs that more effectively meet practical application requirements. Moreover, we suspect the difference in the mode covering versus mode seeking in the active learning versus RL may also be a reason for the difference in the performance [26, 65].

Materials generative models are typically trained on equilibrium or near equilibrium structures, which only represent a small fraction of the chemical space. Incorporating non-equilibrium structures into the training process can improve model robustness and enhance the model’s capability to generate novel structures. Reinforcement fine-tuning achieves this by using MLIP reward model to penalize the unstable structures generated by the model. Alternatively, the direct preference optimization [66] algorithm may be employed to fine-tune the model on pairs of equilibrium and non-equilibrium structures, which eliminates the necessity of training an explicit reward model for material stability.

The stability verifications presented in Fig. 3 and Fig. 6(b) are based on the energy above the convex hull evaluated with an MLIP. This reveals a fundamental challenge in the application of RL in materials science: what is the verifiable ground truth reward signal. Given the intricacies involved in material synthesis and characterization [67], such a challenge is particularly concerning as faulty reward functions [68] which fails to align with the final goal will suggest structures with high reward but fail for the final experiment or even intermediate DFT verifications. We believe the design of reward functions that are both actionable and well-aligned with experimental outcomes, with the insights of human experts, is crucial for ensuring the reliability of the present and many related efforts.

Compared to property-guided material generation based on training on labeled data [3, 69–71], the approaches advertised in [5] (MCMC) and the present work (Reinforcement fine-tuning, also known as variational Bayes) rely on the external discriminative model in a plug-and-play manner. The flexibility and modularity nature of this approach allows seamless integration with many existing and very strong MLIP and ML property prediction models into the materials generative design workflow.

This study focuses on how generative models can be en-

hanced and specialized through the integration of property prediction models. However, the reverse question: how property prediction models can be improved by leveraging generative models—is also an intriguing question worth future investigation. For example, the Orb models employ a two-stage training framework that integrates generative and supervised learning to achieve state-of-the-art performance [13]. Initially, they are pre-trained as denoising diffusion models on datasets of stable materials. The pre-trained model then serves as the initialization for an MLIP, which is subsequently fine-tuned in a supervised manner to predict the energy, forces, and stress of materials. This approach exemplifies how generative pre-training can enhance the performance of discriminative models such as MLIP. Extending this idea further, Ref. [12] has demonstrated that fine-tuning pretrained MLIP also gives bet-

ter performance for property prediction models.

## ACKNOWLEDGMENTS

We thank Han Wang, Linfeng Zhang, Jian Lv, Hongteng Xu, Shigang Ou, Xiaoshan Luo, Mingzhang Yang, Tianping Ying, and Ling Lu for useful discussions. This project is supported by the National Natural Science Foundation of China under Grants No. T2225018, No. 92270107, No. 12188101, and No. T2121001, National Key Projects for Research and Development of China Grant. No. 2021YFA1400400, and the Strategic Priority Research Program of Chinese Academy of Sciences under Grants No. XDB0500000.

- 
- [1] T. Xie, X. Fu, O.-E. Ganea, R. Barzilay, and T. Jaakkola, (2021), [arXiv:2110.06197 \[cs.LG\]](#).
- [2] R. Jiao, W. Huang, P. Lin, J. Han, P. Chen, Y. Lu, and Y. Liu, (2023), [arXiv:2309.04475 \[cond-mat.mtrl-sci\]](#).
- [3] C. Zeni, R. Pinsler, D. Zügner, A. Fowler, M. Horton, X. Fu, Z. Wang, A. Shysheya, J. Crabbé, S. Ueda, *et al.*, *Nature* **639**, 624 (2025).
- [4] N. Gruver, A. Sriram, A. Madotto, A. G. Wilson, C. L. Zitnick, and Z. Ulissi, (2024), [arXiv:2402.04379 \[cs.LG\]](#).
- [5] Z. Cao, X. Luo, J. Lv, and L. Wang, (2024), [arXiv:2403.15734 \[cond-mat.mtrl-sci\]](#).
- [6] R. Jiao, W. Huang, Y. Liu, D. Zhao, and Y. Liu, (2024), [arXiv:2402.03992 \[cs.LG\]](#).
- [7] O. T. Unke, S. Chmiela, H. E. Sauceda, M. Gastegger, I. Poltavsky, K. T. Schütt, A. Tkatchenko, and K.-R. Müller, *Chemical Reviews* **121**, 10142 (2021).
- [8] L. Zhang, J. Han, H. Wang, R. Car, and W. E, *Phys. Rev. Lett.* **120**, 143001 (2018).
- [9] S. Batzner, A. Musaelian, L. Sun, M. Geiger, J. P. Mailoa, M. Kornbluth, N. Molinari, T. E. Smidt, and B. Kozinsky, *Nature communications* **13**, 2453 (2022).
- [10] I. Batatia, D. P. Kovacs, G. Simm, C. Ortner, and G. Csányi, *Advances in neural information processing systems* **35**, 11423 (2022).
- [11] D. Zhang, H. Bi, F.-Z. Dai, W. Jiang, L. Zhang, and H. Wang, (2022), [arXiv:2208.08236 \[physics.chem-ph\]](#).
- [12] D. Zhang, X. Liu, X. Zhang, C. Zhang, C. Cai, H. Bi, Y. Du, X. Qin, J. Huang, B. Li, Y. Shan, J. Zeng, Y. Zhang, S. Liu, Y. Li, J. Chang, X. Wang, S. Zhou, J. Liu, X. Luo, Z. Wang, W. Jiang, J. Wu, Y. Yang, J. Yang, M. Yang, F.-Q. Gong, L. Zhang, M. Shi, F.-Z. Dai, D. M. York, S. Liu, T. Zhu, Z. Zhong, J. Lv, J. Cheng, W. Jia, M. Chen, G. Ke, W. E, L. Zhang, and H. Wang, (2023), [arXiv:2312.15492 \[physics.chem-ph\]](#).
- [13] M. Neumann, J. Gin, B. Rhodes, S. Bennett, Z. Li, H. Choubisa, A. Hussey, and J. Godwin, (2024), [arXiv:2410.22570 \[cond-mat.mtrl-sci\]](#).
- [14] T. Xie and J. C. Grossman, *Phys. Rev. Lett.* **120**, 145301 (2018).
- [15] C. Chen, W. Ye, Y. Zuo, C. Zheng, and S. P. Ong, *Chemistry of Materials* **31**, 3564 (2019).
- [16] S. Dathathri, A. Madotto, J. Lan, J. Hung, E. Frank, P. Molino, J. Yosinski, and R. Liu, (2019), [arXiv:1912.02164 \[cs.CL\]](#).
- [17] P. Dhariwal and A. Nichol, (2021), [arXiv:2105.05233 \[cs.LG\]](#).
- [18] L. Ouyang, J. Wu, X. Jiang, D. Almeida, C. Wainwright, P. Mishkin, C. Zhang, S. Agarwal, K. Slama, A. Ray, *et al.*, *Advances in neural information processing systems* **35**, 27730 (2022).
- [19] D. M. Ziegler, N. Stiennon, J. Wu, T. B. Brown, A. Radford, D. Amodei, P. Christiano, and G. Irving, *arXiv preprint arXiv:1909.08593* (2019).
- [20] R. S. Sutton and A. G. Barto, *Reinforcement Learning: An Introduction*, 2nd ed. (MIT Press, 2018).
- [21] DeepSeek AI, (2025), [arXiv:2501.12948 \[cs.CL\]](#).
- [22] See <https://github.com/deepmodeling/CrystalFormer> for code and model checkpoint.
- [23] J. Schulman, X. Chen, and P. Abbeel, *arXiv preprint arXiv:1704.06440* (2017).
- [24] N. Jaques, S. Gu, D. Bahdanau, J. M. Hernández-Lobato, R. E. Turner, and D. Eck, in *International Conference on Machine Learning* (PMLR, 2017) pp. 1645–1654.
- [25] T. Korbak, E. Perez, and C. L. Buckley, (2022), [arXiv:2205.11275 \[cs.LG\]](#).
- [26] S. Levine, (2018), [arXiv:1805.00909 \[cs.LG\]](#).
- [27] S.-H. Li and L. Wang, *Phys. Rev. Lett.* **121**, 260601 (2018).
- [28] D. Wu, L. Wang, and P. Zhang, *Phys. Rev. Lett.* **122**, 080602 (2019).
- [29] J. Schulman, F. Wolski, P. Dhariwal, A. Radford, and O. Klimov, (2017), [arXiv:1707.06347 \[cs.LG\]](#).
- [30] C. Chen and S. P. Ong, *Nature Computational Science* **2**, 718 (2022).
- [31] I. Batatia, P. Benner, Y. Chiang, A. M. Elena, D. P. Kovács, J. Riebesell, X. R. Advincula, M. Asta, M. Avaylon, W. J. Baldwin, F. Berger, N. Bernstein, A. Bhowmik, S. M. Blau, V. Cărare, J. P. Darby, S. De, F. D. Pia, V. L. Deringer, R. Elijošius, Z. El-Machachi, F. Falcioni, E. Fako, A. C. Ferrari, A. Genreith-Schriever, J. George, R. E. A. Goodall, C. P. Grey, P. Grigorev, S. Han, W. Handley, H. H. Heenen, K. Hermansson, C. Holm, J. Jaafar, S. Hofmann, K. S. Jakob, H. Jung, V. Kapil, A. D. Kaplan, N. Karimitari, J. R. Kermode, N. Kroupa, J. Kullgren, M. C. Kuner, D. Kuryla, G. Liepuoniute, J. T. Margraf, I.-B. Magdău, A. Michaelides, J. H. Moore, A. A. Naik, S. P. Niblett, S. W. Norwood, N. O’Neill, C. Ortner, K. A. Persson, K. Reuter, A. S. Rosen, L. L. Schaaf, C. Schran, B. X. Shi, E. Sivonxay, T. K. Stenczel, V. Svahn, C. Sutton, T. D. Swinburne, J. Tilly, C. van der Oord, E. Varga-Umbrich, T. Vegge, M. Vondrák, Y. Wang, W. C. Witt, F. Zills,



- and G. Csányi, (2024), [arXiv:2401.00096 \[physics.chem-ph\]](#).
- [32] H. Yang, C. Hu, Y. Zhou, X. Liu, Y. Shi, J. Li, G. Li, Z. Chen, S. Chen, C. Zeni, M. Horton, R. Pinsler, A. Fowler, D. Züchner, T. Xie, J. Smith, L. Sun, Q. Wang, L. Kong, C. Liu, H. Hao, and Z. Lu, (2024), [arXiv:2405.04967 \[cond-mat.mtrl-sci\]](#).
- [33] H. Park, S. Majumdar, X. Zhang, J. Kim, and B. Smit, *Digital Discovery* **3**, 728 (2024).
- [34] M. Thomas, A. Bou, and G. D. Fabritiis, (2025), [arXiv:2501.15971 \[cs.LG\]](#).
- [35] M. Popova, O. Isayev, and A. Tropsha, *Science Advances* **4**, 10.1126/sciadv.aap7885 (2018).
- [36] E. Mazuz, G. Shtar, B. Shapira, and L. Rokach, *Scientific Reports* **13**, 8799 (2023).
- [37] J. Schmidt, T. F. Cerqueira, A. H. Romero, A. Loew, F. Jäger, H.-C. Wang, S. Botti, and M. A. Marques, *Materials Today Physics* **48**, 101560 (2024).
- [38] J. Riebesell, R. E. A. Goodall, P. Benner, Y. Chiang, B. Deng, A. A. Lee, A. Jain, and K. A. Persson, (2024), [arXiv:2308.14920 \[cond-mat.mtrl-sci\]](#).
- [39] We sample space group index following the same distribution of the training dataset and use it as precondition to the CrystalFormer.
- [40] V. S. Urusov and T. N. Nadezhina, *Journal of Structural Chemistry* **50**, 22 (2009).
- [41] B. Wang, W. Huang, L. Chi, M. Al-Hashimi, T. Marks, and A. Facchetti, *Chemical Reviews* **118**, 5690 (2018).
- [42] R. P. Ortiz, A. Facchetti, and T. J. Marks, *Chemical Reviews* **110**, 205 (2010), pMID: 19852443, <https://doi.org/10.1021/cr9001275>.
- [43] C. Chen, Y. Zuo, W. Ye, X. Li, and S. P. Ong, *Nature Computational Science* **1**, 46 (2021).
- [44] J. Riebesell, T. W. Surta, R. Goodall, M. Gaultois, and A. A. Lee, (2024), [arXiv:2401.05848 \[cond-mat.mtrl-sci\]](#).
- [45] A. Jain, S. P. Ong, G. Hautier, W. Chen, W. D. Richards, S. Dacek, S. Cholia, D. Gunter, D. Skinner, G. Ceder, and K. A. Persson, *APL Materials* **1**, 011002 (2013).
- [46] I. Petousis, D. Mrdjenovich, E. Ballouz, M. Liu, D. Winston, W. Chen, T. Graf, T. D. Schladt, K. A. Persson, and F. B. Prinz, *Scientific data* **4**, 1 (2017).
- [47] S. Falletta, A. Cepellotti, A. Johansson, C. W. Tan, A. Musaelian, C. J. Owen, and B. Kozinsky, (2024), [arXiv:2403.17207 \[cond-mat.mtrl-sci\]](#).
- [48] N. R. Wolf, B. A. Connor, A. H. Slavney, and H. I. Karunadasa, *Angewandte Chemie* **133**, 16400 (2021).
- [49] A. Merchant, S. Batzner, S. S. Schoenholz, M. Aykol, G. Cheon, and E. D. Cubuk, *Nature* **624**, 80 (2023).
- [50] J. Leeman, Y. Liu, J. Stiles, S. B. Lee, P. Bhatt, L. M. Schoop, and R. G. Palgrave, *PRX Energy* **3**, 011002 (2024).
- [51] L. Hanebali, T. Machej, C. Cros, and P. Hagenmuller, *Materials Research Bulletin* **16**, 887 (1981).
- [52] K. Suzuki, *Journal of the Physical Society of Japan* **16**, 67 (1961).
- [53] B. Póta, P. Ahlawat, G. Csányi, and M. Simoncelli, *Thermal conductivity predictions with foundation atomistic models* (2024), [arXiv:2408.00755 \[cond-mat.mtrl-sci\]](#).
- [54] A. Loew, D. Sun, H.-C. Wang, S. Botti, and M. A. L. Marques, *Universal machine learning interatomic potentials are ready for phonons* (2024), [arXiv:2412.16551 \[cond-mat.mtrl-sci\]](#).
- [55] X. Fu, B. M. Wood, L. Barroso-Luque, D. S. Levine, M. Gao, M. Dzamba, and C. L. Zitnick, [arXiv preprint arXiv:2502.12147](#) (2025).
- [56] D. Flam-Shepherd and A. Aspuru-Guzik, (2023), [arXiv:2305.05708 \[cs.LG\]](#).
- [57] L. M. Antunes, K. T. Butler, and R. Grau-Crespo, *Nature Communications* **15**, 1 (2024).
- [58] L. Zhang, A. Rao, and M. Agrawala, (2023), [arXiv:2302.05543 \[cs.CV\]](#).
- [59] Y. Fan and K. Lee, (2024), [arXiv:2301.13362 \[cs.LG\]](#).
- [60] K. Black, M. Janner, Y. Du, I. Kostrikov, and S. Levine, (2024), [arXiv:2305.13301 \[cs.LG\]](#).
- [61] Y. Fan, O. Watkins, Y. Du, H. Liu, M. Ryu, C. Boutilier, P. Abbeel, M. Ghavamzadeh, K. Lee, and K. Lee, (2023), [arXiv:2305.16381 \[cs.LG\]](#).
- [62] X.-Q. Han, Z. Ouyang, P.-J. Guo, H. Sun, Z.-F. Gao, and Z.-Y. Lu, *Chin. Phys. Lett.* (2025).
- [63] Z. Li, S. Liu, B. Ye, D. J. Srolovitz, and T. Wen, *Active learning for conditional inverse design with crystal generation and foundation atomic models* (2025), [arXiv:2502.16984 \[cond-mat.mtrl-sci\]](#).
- [64] Z. Shao, P. Wang, Q. Zhu, R. Xu, J. Song, X. Bi, H. Zhang, M. Zhang, Y. K. Li, Y. Wu, and D. Guo, (2024), [arXiv:2402.03300 \[cs.CL\]](#).
- [65] I. Goodfellow, Y. Bengio, and A. Courville, *Deep Learning* (MIT Press, 2016) <http://www.deeplearningbook.org>.
- [66] R. Rafailov, A. Sharma, E. Mitchell, S. Ermon, C. D. Manning, and C. Finn, (2024), [arXiv:2305.18290 \[cs.LG\]](#).
- [67] A. K. Cheetham and R. Seshadri, *Chemistry of Materials* **36**, 3490 (2024).
- [68] J. Clark and D. Amodei, *Faulty reward functions in the wild* (2016).
- [69] R. Gómez-Bombarelli, J. N. Wei, D. Duvenaud, J. M. Hernández-Lobato, B. Sánchez-Lengeling, D. Sheberla, J. Aguilera-Iparraguirre, T. D. Hirzel, R. P. Adams, and A. Aspuru-Guzik, *ACS Central Science* **4**, 268 (2018), pMID: 29532027.
- [70] C.-Y. Ye, H.-M. Weng, and Q.-S. Wu, *Computational Materials Today* **1**, 100003 (2024).
- [71] X. Luo, Z. Wang, P. Gao, J. Lv, Y. Wang, C. Chen, and Y. Ma, *npj Computational Materials* **10**, 254 (2024).
- [72] J. Su, Y. Lu, S. Pan, A. Murtadha, B. Wen, and Y. Liu, (2023), [arXiv:2104.09864 \[cs.CL\]](#).
- [73] D. P. Kingma and J. Ba, (2017), [arXiv:1412.6980 \[cs.LG\]](#).
- [74] <https://huggingface.co/datasets/zdcao/alex-20>.
- [75] S. Mohamed, M. Rosca, M. Figurnov, and A. Mnih, *Journal of Machine Learning Research* **21**, 1 (2020).
- [76] R. J. Williams, *Machine learning* **8**, 229 (1992).
- [77] Z. Liu, C. Chen, W. Li, P. Qi, T. Pang, C. Du, W. S. Lee, and M. Lin, *Understanding r1-zero-like training: A critical perspective*, <https://github.com/sail-sg/understand-r1-zero> (2025).
- [78] B. Deng, P. Zhong, K. Jun, J. Riebesell, K. Han, C. J. Bartel, and G. Ceder, (2023), [arXiv:2302.14231 \[cond-mat.mtrl-sci\]](#).
- [79] S. P. Ong, W. D. Richards, A. Jain, G. Hautier, M. Kocher, S. Cholia, D. Gunter, V. L. Chevrier, K. A. Persson, and G. Ceder, *Computational Materials Science* **68**, 314 (2013).
- [80] K. F. Young and H. P. R. Frederikse, *Journal of Physical and Chemical Reference Data* **2**, 313 (1973).
- [81] T. W. Ko, M. Nassar, S. Miret, E. Liu, J. Qi, and S. P. Ong, *Materials Graph Library* (2021).
- [82] Z. Mao, W. Li, and J. Tan, (2024), [arXiv:2405.09052 \[cond-mat.mtrl-sci\]](#).



### Appendix A: The CrystalFormer model card

The architecture of CrystalFormer is identical to the one described in Ref. [5], except for an update on the positional encoding. We use the rotary positional encoding (RoPE) [72] instead of the absolute positional encoding in the original design.

The base model was trained for 5500 epochs with a total batch size of 8000 over eight A100 GPUs using the Adam optimizer [73]. The learning rate was set to  $8e - 4$ .

The reinforcement fine-tuning was performed for 100 - 200 steps, depending on the task. For the reinforcement fine-tuning, we use a total batch size of 1000 over two A100 GPUs and the Adam optimizer with a learning rate of  $1e - 4$ . The pre-training phase required approximately 1000 GPU hours, while the reinforcement fine-tuning phase took around 12 to 24 GPU hours.

For the supervised fine-tuning (SFT) of the CrystalFormer, we generate 10,000 crystal samples and relax them using the Orb models. Only those stable samples with  $E_{\text{hull}} < 0.1$  eV/atom were retained for SFT. The SFT was performed for 55 epochs when validation loss stopped improving, with a batch size of 100 using the Adam optimizer with a learning rate of  $1e - 5$  on a single A100 GPU.

Table S1. A table of hyperparameters used in this work.

Hyperparameters	Value	Remarks
The length of atom sequence including the padding atoms	21	
Number of chemical species	119	'H' to 'Og', plus padding atom
Number of possible Wyckoff letters	28	'a-z'+ 'A', plus padding atom
Number of modes in von-Mises mixture distribution $K_x$	16	
Number of modes in lattice Gaussian mixture distribution $K_l$	4	
Hidden layer dimension for the composite type of the first atom	256	
Transformer number of layers	16	
Transformer number of heads	16	
Transformer key size	64	
Transformer model size $d_{\text{model}}$	64	
Embedding dimension of discrete input	32	
Number of Fourier frequency $N_f$	5	
Dropout rate in pre-training	0.1	No dropout in fine-tuning
Gradient clipping	1	
RL regularization coefficient $\tau$	0.1	15 for FoM reward
PPO clipping parameter $\epsilon$	0.2	
PPO steps between resampling	3	
Total number of parameters: 4833575		

## Appendix B: Training dataset

The Alexandria dataset [37] was chosen as a starting point because it was the largest openly available DFT dataset of equilibrium and near equilibrium structures ( $\sim 4.5$  million materials). Using the same criteria as MatterGen [3] (distances to the convex hull less than 0.1 eV/atom and less than 20 atoms in the unit cell), Alexandria now contains more than 1.3 million materials. 80% of the data set was used for training and the remaining were divided equally between validation and test datasets. The Alex-20 dataset is available at [74].

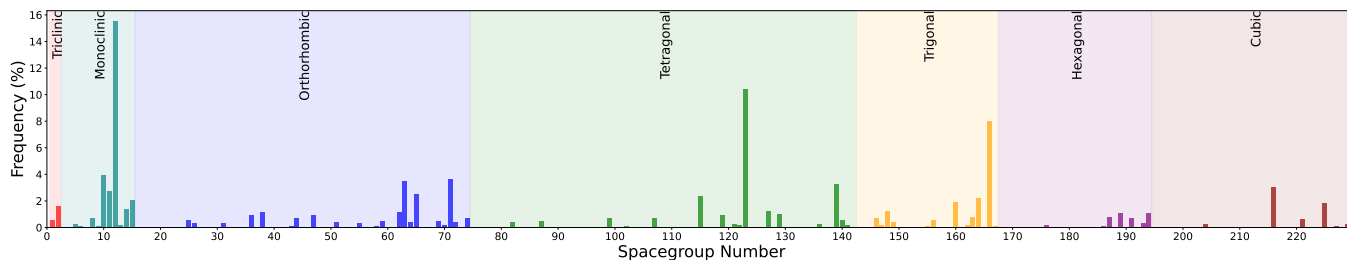


Figure S1. Space group distribution of the Alex-20 dataset.

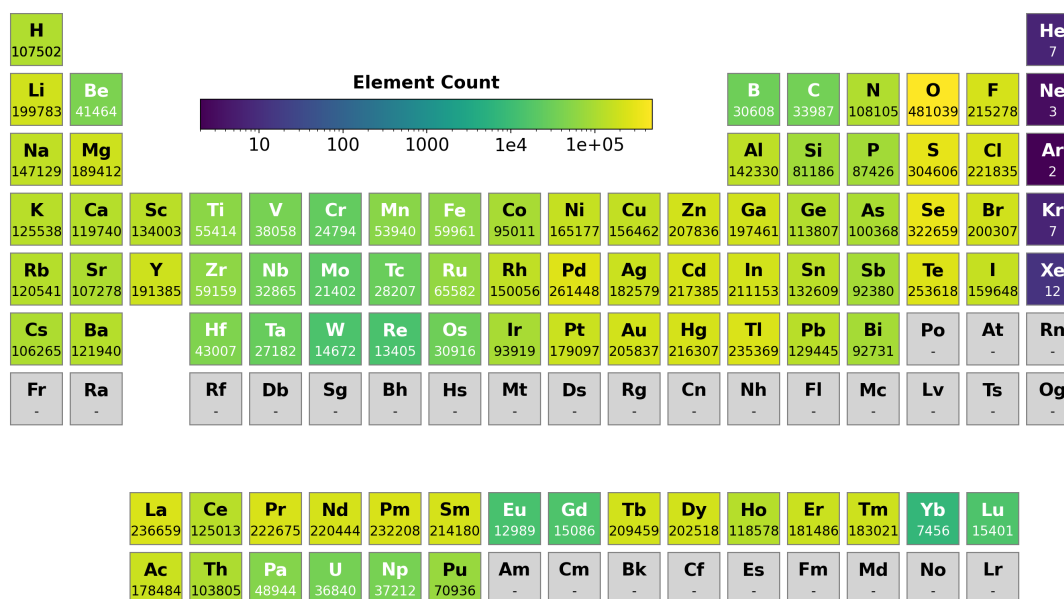


Figure S2. Distribution of elements in Alex-20.

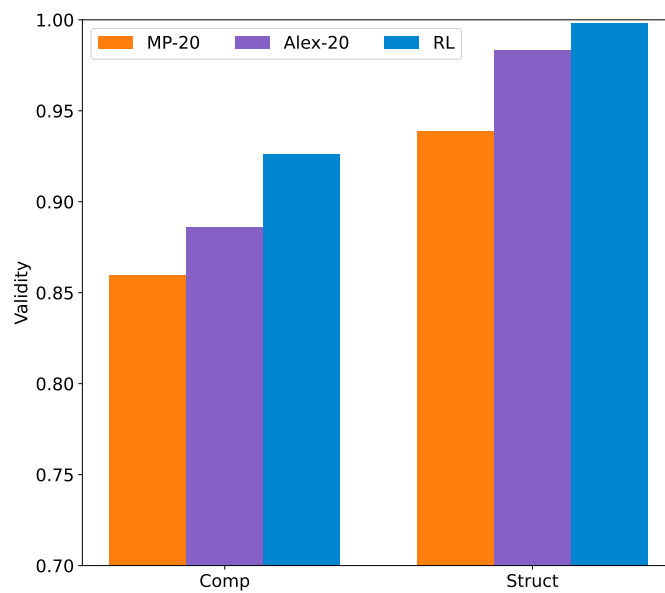


Figure S3. Composition and structure validity of samples generated by the pretrained CrystalFormer using the MP-20 and Alex-20 dataset, as well as RL fine-tuned model.

### Appendix C: Details of reinforcement fine-tuning implementation

The proximal policy optimization (PPO) [29] is a simple yet effective policy gradient-based RL algorithm. The algorithm optimizes the following objective function,

$$\mathcal{L}^{\text{PPO}}(\theta) = \mathbb{E}_{x \sim p_{\text{old}}(x)} [\min(\gamma(\theta)A(x), \text{clip}(\gamma(\theta), 1 - \epsilon, 1 + \epsilon))A(x)], \tag{S1}$$

where  $\gamma(\theta) = \frac{p_{\theta}(x)}{p_{\text{old}}(x)}$  denotes the probability ratio between the policy under optimization and the policy for sampling,  $A(x)$  is the advantage function, and  $\epsilon$  is the clipping parameter. The second term,  $\text{clip}(\gamma(\theta), 1 - \epsilon, 1 + \epsilon)$ , modifies the surrogate objective by clipping the probability ratio, which removes the incentive for moving  $\gamma(\theta)$  outside of the interval  $[1 - \epsilon, 1 + \epsilon]$ . Drawing samples from  $p_{\text{old}}(x)$  rather than  $p_{\theta}(x)$  stems from the importance sampling and reduce the number of costly evaluation of the reward function.

We use  $R(x)$  denotes the reward function with entropy regularization,

$$R(x) = r(x) - \tau \ln \frac{p_{\theta}(x)}{p_{\text{base}}(x)}. \tag{S2}$$

The advantage function  $A(x)$  is then defined as

$$A(x) = R(x) - b, \tag{S3}$$

where  $b$  represents the baseline. Note that one does not need to compute the gradient of  $A(x)$  with respect to network parameters  $\theta$  in the PPO algorithm. Instead, one uses the score function gradient estimate [75] to maximize the objective function  $\mathcal{L}^{\text{PPO}}(\theta)$ . For each batch of samples from  $p_{\text{old}}$  and reward signal, we carry out a few gradient ascent steps to update the policy network. The detailed hyperparameters used in the PPO algorithm are listed in Table S1.

The advantage function measures the deviation of the reward  $R(x)$  from this baseline, indicating how much better or worse the generated samples is compared to the baseline. In standard PPO implementations, this baseline is typically approximated by a value function, which is trained alongside the policy model. We use the average reward of the generated samples  $x$ , i.e.,  $b = \mathbb{E}_{x \sim p_{\text{old}}}[R(x)]$  as the baseline [76]. This approach obviates the need for training a separate value function and is equivalent to the group relative policy optimization done right [64, 77].

For the baseline  $b$  we use an exponential moving average of the previous rewards, which stabilizes the training and also leverages the past reward information to form a lagged baseline. To be more specific, the baseline is updated as  $b_k = \eta b_{k-1} + (1 - \eta)\bar{R}_k$ , where  $\eta = 0.95$  and  $b_0$  is initialized as the average reward of the initial batch  $\bar{R}_0$ . Here,  $\bar{R}_k$  is the average reward of the current batch.

We employ the Orb-v2 [13] trained on the MPTraj [78] and Alexandria dataset [37] to as the reward model for energy prediction for the generated samples. We calculate the energy above the convex hull using the energy predicted by the Orb model in the Materials Project energy correction framework (i.e., `MaterialsProject2020Compatibility` from `pymatgen` [79]).



### Appendix D: Dielectric constant prediction model

The total dielectric constant is defined as

$$\epsilon_{\text{total}} = \epsilon_{\text{ionic}} + \epsilon_{\text{elec}}, \quad (\text{S1})$$

where  $\epsilon_{\text{ionic}}$  and  $\epsilon_{\text{elec}}$  denote the ionic and electronic contributions to the dielectric constant, respectively. In fact, the dielectric constant is fundamentally a tensor  $\epsilon_{ij}$ , and the scalar dielectric constant  $\epsilon_{\text{total}}$  is the mean of the eigenvalues of the total dielectric tensor. The dielectric tensor can be written as

$$\epsilon = \begin{bmatrix} \epsilon_{11} & \epsilon_{12} & \epsilon_{13} \\ \epsilon_{21} & \epsilon_{22} & \epsilon_{23} \\ \epsilon_{31} & \epsilon_{32} & \epsilon_{33} \end{bmatrix}, \quad (\text{S2})$$

where  $\epsilon_{12} = \epsilon_{21}$ ,  $\epsilon_{13} = \epsilon_{31}$ , and  $\epsilon_{23} = \epsilon_{32}$ . While the dielectric tensor is characterized by 9 components, only up to 6 are independent elements. Moreover, this number decreases with higher material symmetry [80].

We use the M3GNet [30] model implemented in the MatGL [81] repository to predict the 6 independent components of the total dielectric tensor using the DFPT calculations in Materials Project dataset [45, 46]. The 6 independent components were predicted by the model and assembled into a  $3 \times 3$  matrix, from which the total dielectric constant was determined by solving for its eigenvalues. Following the data processing in Ref. [82], we clean up the dataset by restricting the components in total dielectric constants  $\epsilon_{ij} \in [-10, 100]$  for  $\forall i, j$ , which resulted in a dataset of  $\sim 7,000$  structures. The above dataset is then divided into training, validation, and test subsets with a ratio of 8:1:1, respectively, for the purpose of experimental analysis. The dielectric property prediction model is trained with the  $L1$  loss and batch size of 64 and learning rate of  $1e-4$ , using the Adam optimizer with default parameters. Other training settings remained as the default configuration of MatGL.

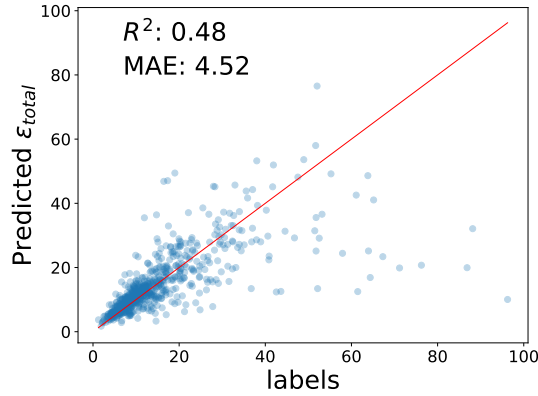


Figure S4. Performance of M3GNet on the test set of our refined MP dataset for  $\epsilon_{\text{total}}$ .

Figure S4 illustrated the performance of M3GNet on the by calculating the total dielectric constant. It can be observed that despite constraining the data range, the model's generalization within this range remains limited, often underestimating the total dielectric constant of the materials. This issue can be resolved by implementing a more robust prediction model or by expanding the dataset to include a broader range of dielectric constants.

### Appendix E: Dielectric materials discovered by CrystalFormer-RL

As summarized in the Table S2, the reinforcement fine-tuned model generates a series of stable dielectric materials with high FoM values, with only two samples present in the DFPT dataset. The labels of the  $\text{LiTi}_2\text{InF}_6$  compound are band gap 4.10 eV and total dielectric constant 27.49. The labels of  $\text{Ba}_2\text{TaFeO}_6$  are band gap 1.86 eV and total dielectric constant 46.92. Both are close to the predicted values in Table S2.

Table S2. Dielectric materials discovered by CrystalFormer-RL, ranked according to their figures of merit (FoM):  $\epsilon_{\text{total}} \cdot E_g$ . See details of the samples at [https://drive.google.com/file/d/1ouz0RRgntiSoVRe5VP\\_cemnAdcb3MpTj/view?usp=sharing](https://drive.google.com/file/d/1ouz0RRgntiSoVRe5VP_cemnAdcb3MpTj/view?usp=sharing).

Formula	$E_g$ (eV) <sup>1</sup>	$\epsilon_{\text{total}}$ <sup>1</sup>	FoM (eV)	$E_{\text{hull}}$ (eV/atom) <sup>2</sup>	Not in Alex-20	Not in DFPT dataset
$\text{LiNdTi}_2\text{F}_6$	4.54	41.73	189.54	0.09		✓
$\text{LiLaTi}_2\text{F}_6$	4.48	40.44	181.35	0.08		✓
$\text{LiErTi}_2\text{F}_6$	4.73	36.56	172.78	0.05		✓
$\text{LiScTi}_2\text{F}_6$	4.40	37.41	164.57	0.03		✓
$\text{K DyTi}_2\text{F}_6$	6.32	23.49	148.50	0.05	✓	✓
$\text{Na TbTi}_2\text{F}_6$	5.02	29.17	146.56	0.02	✓	✓
$\text{Li YTi}_2\text{F}_6$	4.69	30.98	145.27	0.04		✓
$\text{Li TmTi}_2\text{F}_6$	4.53	29.19	132.27	0.03		✓
$\text{Li NiPb}_2\text{F}_6$	4.12	30.43	125.26	-0.04	✓	✓
$\text{Li}_6\text{PbCl}_8$	4.64	25.19	116.76	0.08	✓	✓
$\text{Cs}_2\text{BaSrF}_6$	5.38	21.32	114.75	0.04	✓	✓
$\text{Cs}_2\text{SmTiF}_6$	5.69	20.12	114.50	0.02		✓
$\text{La MnTi}_2\text{F}_6$	3.03	36.01	109.15	-0.04	✓	✓
$\text{Cs}_2\text{SrCaF}_6$	6.10	17.86	108.92	0.01		✓
$\text{Cs}_2\text{LiNdF}_6$	6.44	16.90	108.90	0.06		✓
$\text{ScTi}_2\text{WO}_6$	1.99	54.47	108.50	0.10	✓	✓
$\text{ScPb}_2\text{WO}_6$	1.53	70.52	107.90	0.10	✓	✓
$\text{Ba}_2\text{TaMnO}_6$	2.75	39.00	107.37	0.08		✓
$\text{CsBaF}_3$	5.81	18.38	106.78	0.08		✓
$\text{LiTi}_2\text{InF}_6$	3.72	28.74	106.76	0.03		
$\text{Cs}_2\text{LiPrF}_6$	6.52	16.25	105.99	0.07		✓
$\text{Rb}_2\text{NdTiF}_6$	5.29	20.02	105.90	0.09	✓	✓
$\text{Ba}_2\text{TaFeO}_6$	2.07	50.19	103.81	0.02	✓	
$\text{Cs}_2\text{ScTiF}_6$	4.87	21.26	103.51	0.00		✓
$\text{Cs}_2\text{LiLaF}_6$	5.96	17.35	103.50	0.07		✓
$\text{Cs}_2\text{KNdF}_6$	5.96	17.37	103.49	0.01		✓
$\text{Cs}_2\text{RbNdF}_6$	6.40	16.16	103.49	0.02		✓
$\text{Cs}_2\text{BaCaF}_6$	6.07	17.00	103.13	0.04		✓
$\text{Cs}_2\text{LuTiF}_6$	5.48	18.61	101.96	0.00	✓	✓
$\text{Cs}_2\text{BaPbF}_6$	4.66	21.82	101.69	0.04		✓
$\text{Cs}_2\text{RbSrF}_6$	5.89	17.22	101.47	0.09		✓
$\text{Cs}_3\text{NdF}_6$	6.18	16.33	100.95	0.04		✓

<sup>1</sup> The band gap and total dielectric constant are predicted by machine learning models.

<sup>2</sup> The energy above the convex hull is computed via the Orb model based on Alexandria convex hull.

Table S3. Dielectric materials discovered in the Alex-20 dataset. Superscript 'eq' denotes the prediction results for equilibrium structure in the Alex-20 dataset

Formula	$E_g$ (eV) <sup>1</sup>	$\epsilon_{total}$ <sup>1</sup>	FoM (eV)	$a$ (Å) <sup>2</sup>	$E_g^{eq}$ (eV) <sup>1</sup>	$\epsilon_{total}^{eq}$ <sup>1</sup>	FoM <sup>eq</sup> (eV)	$a^{eq}$ (Å) <sup>2</sup>
LiNdTi <sub>2</sub> F <sub>6</sub>	4.54	41.73	189.54	6.23	4.69	41.92	196.41	6.23
LiLaTi <sub>2</sub> F <sub>6</sub>	4.48	40.44	181.35	6.31	4.63	37.72	174.53	6.22
LiErTi <sub>2</sub> F <sub>6</sub>	4.73	36.56	172.78	6.09	4.71	36.93	173.98	6.11
LiScTi <sub>2</sub> F <sub>6</sub>	4.40	37.41	164.57	6.00	4.54	36.24	164.49	6.00
LiYTi <sub>2</sub> F <sub>6</sub>	4.69	30.98	145.27	6.16	4.70	30.31	142.52	6.13
LiTmTi <sub>2</sub> F <sub>6</sub>	4.53	29.19	132.27	6.09	4.59	29.99	137.59	6.09
Cs <sub>2</sub> SmTiF <sub>6</sub>	5.69	20.12	114.50	7.11	5.73	19.84	113.69	7.01
Cs <sub>2</sub> SrCaF <sub>6</sub>	6.10	17.86	108.92	6.73	6.04	16.59	100.17	6.64
Cs <sub>2</sub> LiNdF <sub>6</sub>	6.44	16.90	108.90	6.41	6.41	16.82	107.89	6.41
Ba <sub>2</sub> TaMnO <sub>6</sub>	2.75	39.00	107.37	5.85	1.88	35.08	65.82	5.66
CsBaF <sub>3</sub>	5.81	18.38	106.78	7.34	5.81	18.94	109.98	5.14
LiTi <sub>2</sub> InF <sub>6</sub>	3.72	28.74	106.76	6.06	3.90	26.52	103.32	6.05
Cs <sub>2</sub> LiPrF <sub>6</sub>	6.52	16.25	105.99	6.46	6.43	15.79	101.48	6.43
Cs <sub>2</sub> ScTiF <sub>6</sub>	4.87	21.26	103.51	6.82	4.86	20.78	100.99	6.73
Cs <sub>2</sub> LiLaF <sub>6</sub>	5.96	17.35	103.50	6.45	5.68	16.72	94.88	6.44
Cs <sub>2</sub> KNdF <sub>6</sub>	5.96	17.37	103.49	7.03	5.81	14.85	86.31	6.90
Cs <sub>2</sub> RbNdF <sub>6</sub>	6.40	16.16	103.49	7.11	6.45	15.85	102.16	7.04
Cs <sub>2</sub> BaCaF <sub>6</sub>	6.07	17.00	103.13	6.87	6.08	16.77	101.99	6.84
Cs <sub>2</sub> BaPbF <sub>6</sub>	4.66	21.82	101.69	7.14	4.64	21.61	100.23	7.10
Cs <sub>2</sub> RbSrF <sub>6</sub>	5.89	17.22	101.47	7.05	5.41	17.39	94.01	7.07
Cs <sub>3</sub> NdF <sub>6</sub>	6.18	16.33	100.95	7.29	5.18	13.51	69.98	7.22

<sup>1</sup> The band gap and total dielectric constant are predicted by machine learning models.

<sup>2</sup> The lattice constant is measured using the primitive cell.